



HAL
open science

Sub-millisecond microfluidic mixers coupled to time-resolved in situ photonics to study ultra-fast reaction kinetics: the case of ultra-small gold nanoparticle synthesis

Raj Kumar Ramamoorthy, Ezgi Yildirim, Isaac Rodríguez-Ruiz, Pierre Roblin, Lise-Marie Lacroix, Ana Diaz, Rohan Parmar, Sébastien Teychené, Guillaume Viau

► To cite this version:

Raj Kumar Ramamoorthy, Ezgi Yildirim, Isaac Rodríguez-Ruiz, Pierre Roblin, Lise-Marie Lacroix, et al.. Sub-millisecond microfluidic mixers coupled to time-resolved in situ photonics to study ultra-fast reaction kinetics: the case of ultra-small gold nanoparticle synthesis. *Lab on a Chip*, 2024, 10.1039/d3lc00778b . hal-04346488

HAL Id: hal-04346488

<https://hal.science/hal-04346488>

Submitted on 15 Dec 2023

HAL is a multi-disciplinary open access archive for the deposit and dissemination of scientific research documents, whether they are published or not. The documents may come from teaching and research institutions in France or abroad, or from public or private research centers.

L'archive ouverte pluridisciplinaire **HAL**, est destinée au dépôt et à la diffusion de documents scientifiques de niveau recherche, publiés ou non, émanant des établissements d'enseignement et de recherche français ou étrangers, des laboratoires publics ou privés.

Sub-millisecond microfluidic mixers coupled to time-resolved in-situ photonics to study ultra-fast reaction kinetics. The case of ultra-small gold nanoparticles synthesis

Received 14th September 2023,
Accepted 2nd December 2023

DOI: 10.1039/d3lc00778b

Raj Kumar Ramamoorthy,^{1,2,3,†} Ezgi Yildirim,^{1,†} Isaac Rodriguez-Ruiz,^{2,*} Pierre Roblin,² Lise-Marie Lacroix,^{1,5} Ana Diaz,⁴ Rohan Parmar,² Sébastien Teychené,² Guillaume Viau^{1,*}

We report a continuous microreactor platform achieving sub-millisecond homogeneous reagent mixing (~ 300 μs) for a time-resolved study on the synthesis of ultra-small gold nanoparticles (NP). The microreactor (coupled with small angle X-ray scattering, UV-Vis, and X-ray absorption spectroscopy for in-situ and in-operando characterizations), operates within mixing time frames below system characteristic times, providing a unique opportunity to deepen into the comprehension of reaction and phase transition pathways with unprecedented detail. The microreactor channel length can be approximated to a given reaction time when operated in continuous mode and steady state. As a result, the system can be statically interrogated, eliminating technique-dependent probing time constraints and local inhomogeneities caused by mixing issues. We have studied Au(0) NP formation kinetics from Au(III) precursors complexed with oleylamine in organic media, using triisopropylsilane as a reducing agent. The existence of Au(III)/Au(I) prenucleation clusters, and the formation of a transient Au(I) lamellar phase under certain conditions, before the onset of Au(0) formation, have been observed. Taking advantage of the high frequency time-resolved information, we propose and model two different reaction pathways associated with the presence or absence of the Au(I) lamellar phase. In both cases, non-classical pathways leading to the formation of NPs are discussed.

Introduction

Fast phase transitions are ubiquitous phenomena in our everyday life. They are involved in relevant natural biological and geological process, as well as in key steps in numerous and very distinct human activities related to industrial, chemical and technological fields (e.g. formation and stabilization of micro- and nano-emulsions,¹ the development of novel hydrometallurgical practices associated to materials recycling in urban mines,² or the synthesis of nanomaterials for applications in biotechnology, catalysis, optics, or imaging³). The main purpose in most of these processes is, either to produce a controlled population of particles (micelles, droplet, crystals) in terms of physico-chemical properties (structure, morphology,

size distribution, etc), either to control phase transition kinetics to enhance selective product recovery or avoiding undesired by-products. On this basis, the design and control, and thus the understanding of phase transition phenomena is a must, and precipitation/nucleation of solid crystalline phases, which can occur through different pathways,⁴ is a central figure in the game. It is known that these phase transition pathways, and therefore the final product properties, can be affected by several dynamic constraints,⁵ in which intermediate phases can play a vital role. Within these constraints, from both fundamental and applied point of views, to rationalize these pathways it is essential to take into account reagent mixing process and their time and length scales. Indeed, when reaction/transition characteristic times are shorter (or comparable) to those of mixing, reagent inhomogeneities create local heterogeneous conditions having a strong impact on the formation of intermediates and thus on the path followed by the phase transition. This can occur at scales as short as the millisecond and the micron, respectively in time and length, for systems displaying fast transition kinetics.⁶ That leads to ungoverned process in real world applications, and at the same time hinders the fundamental understanding of the systems. This is actually a well-known issue discussed since the last half of the past century,⁷ and still subject of research and rationalization. Several approaches have been proposed in the literature to attain a better product mastering at the micro- and nano- scales. Among them, and compared to conventional methods, microfluidics allow increased reproducibility and sensitivity through space–time yields, selectivity, reaction times and conversions,^{8, 9} thanks to the enhancement of surface-to-

¹ Université de Toulouse, Laboratoire de Physique et Chimie des Nano-Objets UMR 5215 INSA, CNRS, UPS, 135 avenue de Rangueil F-31077 Toulouse cedex 4, France

² Laboratoire de Génie Chimique, Université de Toulouse, CNRS, INP, UPS Toulouse, France

³ Fédération de Recherche FeRMAT, Université de Toulouse, CNRS, INP, INSA, UPS, Toulouse France

⁴ Paul Scherrer Institute, Villigen PSI, Switzerland

⁵ Institut Universitaire de France (IUF), 103 boulevard Saint Michel, 75005 Paris, France

*Corresponding Author:

isaac.rodriguez-ruiz@cnrs.fr, guillaume.viau@insa-toulouse.fr

† R.K.R and E.Y. contributed equally to this work. They both should be considered first authors.

Electronic Supplementary Information (ESI) available: Microfluidic platforms fabrication procedure, set-up description, complementary information regarding TEM, SAXS and UV-Vis characterizations, and detailed kinetic models.. DOI: <https://doi.org/10.1039/d3lc00778b>

volume ratios and a fine thermal control. This advantageous environment has been exploited already for the study and formation of nano-¹⁰ or micro-emulsions for drug encapsulation,¹¹ or for the synthesis of luminescent and plasmonic nanomaterials,¹² where the fine control on anisotropy and size is essential to tune their properties (e.g. high-quality cadmium sulphide,^{13, 14} cadmium selenide,^{15, 16} palladium,¹⁷⁻¹⁹ silver,²⁰⁻²² gold,²³⁻²⁵ copper,²⁶ titania,²⁵ or even CdSe–ZnS core–shell nanoparticles²⁷). Analogously, microfluidics features have been exploited and specifically aimed towards production-targeted gold nanoparticles syntheses.^{28, 29} And in this advantageous context, the implementation of efficient micromixing at the microfluidic scale, and the access to time-resolved evolution of the system have demonstrated to be another lever of action towards a fine control of gold nanoparticles formation conditions.³⁰ By decoupling mixing phenomena and phase transition, we can assure chemical homogeneity along the entire microreactors. Indeed, rapid and efficient microfluidic micromixers³¹⁻⁴¹ appear to be a promising approach to tackle mixing issues, either for homogeneous particle production or to study fast transition kinetics. Yet, the main limitation of microfluidic approaches is the difficulty of attaining in-situ, time-resolved and real time information on the evolution of the systems. While efforts towards this direction are being made on the implementation on non-invasive inline and online spectrometric techniques,³⁰ this information is still and more often inferred by ex situ, off-line analyses. This becomes even more compelling for events occurring at very short time scales, as frequently information acquisition rates are restricted by the detection technique.

Inspired by recent ultra-fast mixing developments previously reported in the literature,⁴² we have conceived and fabricated a microfluidic platform allowing to achieve controllable sub-millisecond homogeneous mixing of reactants, at relatively low pressure losses (3-4 bars). The mixer design is coupled to a continuous reactor, allowing to operate either continuously or in a stop-flow configuration. When operated in continuous mode and steady state, channel length can be approximated to a given reaction time, which can be statically interrogated, thus getting rid of technique-dependent probing times constraints. Moreover, when the platform is operating within mixing time frames below system characteristic times, and hence before any significant interactions, reactions or phase transitions take place, it is possible to track and separate phase nucleation and early growth stages in a completely homogeneous medium, allowing for time-resolved in-situ kinetic studies.

As a proof-of-principle for this methodology, that can be applied to many reactions and systems of interest, we report a study of the synthesis of monodisperse ultra-small gold nanoparticles (NPs, 1-3 nm), because of their high relevance for numerous research fields, ranging from catalysis to biotechnology or microelectronics. Although it is possible to currently establish a relation between their synthesis conditions and their final morphology, there is still a need to deepen into the fundamental comprehension on their formation process.

Presently, the formation of gold NPs has been mostly described by classical nucleation theory, i.e. a metastable equilibrium in which Au(0) monomers attach/detach on growing crystalline nuclei by thermal fluctuations until overpassing a critical size. Nevertheless, recent in-situ SAXS (small-angle X-Ray scattering) and XAS (X-Ray absorption spectroscopy) observations have

shown that gold NPs can also evolve via non-classical pathways involving transient, disordered intermediate phases.⁴³

Ultrasmall NPs are generally obtained with fast reactions. The particles size, polydispersity, shape and atomic structure are dependent on the chemical reaction, nature of the solvent and of the capping agent and several other parameters. All these parameters may have a strong influence on the mechanism of nucleation and growth,^{44, 45} which is a state-of-the-art research topic. The existence of non-crystalline intermediates and subsequent transformation to nanoparticles are known for metal⁴⁶ and also for inorganic nanoparticles in aqueous solution. In this sense, several studies challenged the classical nucleation mechanism,^{43, 45, 47, 48} suggesting that multi-step pathways might be a widespread phenomenon in solution. As the possible nucleation mechanisms are essentially system-dependent and do not necessarily have a universal character, there is a need for a generic tool (ensuring compatibility with all kind of systems and solvents) allowing for the real-time study of the nucleation and growth steps.

We previously reported a fairly simple strategy for the synthesis of ultrasmall icosahedral Au NPs in hexane, allowing for a reaction yield of 100%, and where we identified the presence of pre-nucleation clusters (PNCs).^{43, 49} The size distribution and the structure of the final NPs strongly depend on the reaction kinetics due to the coexistence of two competitive pathways (Fig. 1).

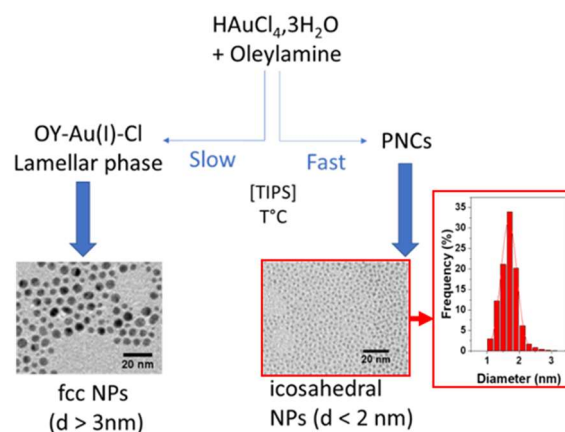


Figure 1. Competitive reaction pathways observed during the reduction of Au(III) precursor by a silane (typically triisopropylsilane – TIPS) in the presence of oleylamine (OY) in organic media. Inset framed in red shows the corresponding size distribution of Au NPs obtained after 3h of reaction in presence of [TIPS] = 1 M

Fast reactions yield monodisperse icosahedral NPs while slower reaction favours the crystallisation of an intermediate Au(I) lamellar phase, which leads to large NPs exhibiting a fcc structure. Interestingly, we have observed that the performance of the synthesis route in terms of particle properties (structure, particle size distribution - PSD) is independent of the type of reactor used for their synthesis, i.e. standard batch reactions, fast stop-flow mixers, or continuous microfluidic reactors, always leading to the results summarized in Fig. 1. This observation, together with the drastic effect of the observed competing reaction pathways on the final NP size and structure, motivates a more detailed study on the very first events of this synthesis, requiring to perform in-situ real-time measurements. In that aim, the previously mentioned microfluidic platform has been fabricated using low cost fabrication procedures.^{50, 51} and

adapted to the specifications of three different spectroscopic characterization techniques: UV-Vis absorption spectroscopy at laboratory facilities using a Photonic Lab-on-a-chip approach,⁸ synchrotron XAS, and SAXS experiments (see materials and methods and supporting information for details). Thanks to submillisecond ($\sim 300 \mu\text{s}$) mixing dead times, and in-situ time-resolved probing, the induction period of the Au NP synthesis, occurring within the first instants of the reaction, was carefully studied revealing its key importance for the system evolution towards one or the other competing reaction pathways.

Experimental

Microfluidic platform specifications, setups and fabrication

Three hybrid platforms with adapted interrogation channel dimensions, were fabricated in OSTEMER (Mercene Labs, Sweden) as a base material,⁵² or in OSTEMER and Kapton, to ensure compatibility with organic media and synchrotron radiations. The platforms were fabricated by injection moulding using PDMS moulds, as described in the supporting information (see Fig. S1 and S2). The PDMS moulds for UV-Vis and SAXS microreactors were fabricated with a low-cost soft-lithographic procedure based on dry film technology, described elsewhere.⁵³ The structure leading to the XAS microreactors, requiring a deeper channel, was fabricated by originally combining resin 3D-printing for millifluidic features with the previously mentioned dry film technology (see Fig. S3 of the supporting information for more details). Fig. 2a shows the schematics of the microreactor. The structure comprises 2 inlets for reagent injection (Fig. 2 A and B), coupled to 2 T-shaped pre mixer and a 4-element butterfly-shape fast mixer structure $20 \mu\text{m} \times 50 \mu\text{m}$ cross-section) adapted from literature.⁴² The structure is conceived for stirring/splitting and recombining fluid streams to achieve fast mixing. Following the mixer, an interrogation (reactor) channel is conceived with a cross section adapted ad-hoc for the specific characterization technique (detailed below).

Both mixer and reaction channel are connected by their two extremes to a bypass (fig. 2c 4) and an outlet channel (fig. 2c 6), connected and controlled by a switch HPLC valve (fig. 2c 7), in a way that it can be operated as a continuous lost flow reactor (fig. 2c 8) by continuously injecting the reagent solutions (for in situ and in operando probing at short reaction times), or as a stop-flow cell (for longer reaction times) if the flowrates are stopped and the outlet is closed simultaneously (fig. 2c 9). Time-resolved information is calculated in continuous operation as a function of reagent flow rates, channels cross section, size of the interrogation beam and its distance from the mixer to the interrogation region, transduced into a reaction time.

Au nanoparticles synthesis

Hydrogen tetrachloroaurate trihydrate ($\text{HAuCl}_4 \cdot 3\text{H}_2\text{O}$, 99.99%, Alfa Aesar), triisopropylsilane (TIPS, 98%, Sigma-Aldrich), oleylamine (OY, 80-90%, Acros) and hexane (mixed isomer, 98+%, Alfa Aesar) were used as purchased. The Au nanoparticles syntheses were performed by reduction of $\text{HAuCl}_4 \cdot 3\text{H}_2\text{O}$ by TIPS in solution of OY in hexane, by keeping a constant final nominal concentration of Au and OY in hexane of 20 mM and 50 mM, respectively. TIPS concentrations were varied from 62 mM to 1 M.

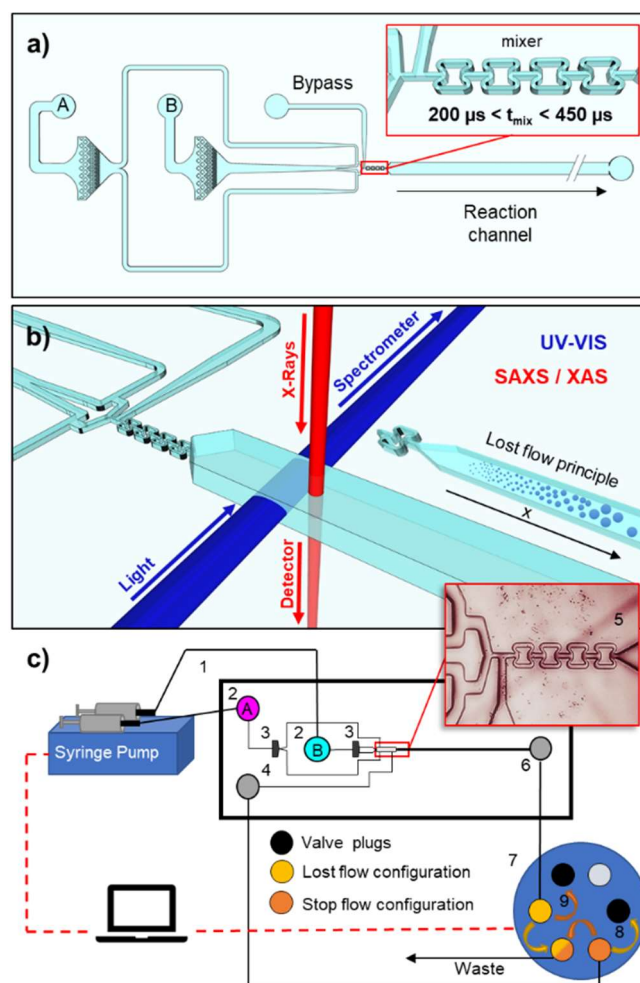
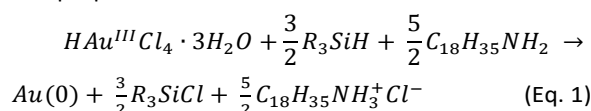


Figure 2. (a) Schematics of the microreactors, comprising two outlets for reagent injection (A, B), a fast passive butterfly-shaped micromixer of cross-section $20 \mu\text{m} \times 50 \mu\text{m}$ (figure inset) and a subsequent interrogation channel for X-ray or UV-visible beam. (b) Operation schematics for the different *in-situ* UV-Vis and SAXS/XAS online microreactors. (c) Experimental setup schematics: 1) OSTEMER Chip; 2) Inlets; 3) Integrated filters; 4) Bypass channel; 5) Butterfly Mixer and main reactor; 6) Outlet 7) Valve 8) Lost Flow Configuration 9) Stop Flow Configuration.

The proposed reaction can be written as:



where oleylamine ($\text{C}_{18}\text{H}_{35}\text{NH}_2$) is used as ligand and the silane (R_3SiH , $\text{R}_3 = \text{ethyl or propyl}$) is always added in excess.

Experimentally, $\text{HAuCl}_4 \cdot 3\text{H}_2\text{O}$ was solubilized in hexane by the addition of OY and sonication, leading to a yellow solution. The solution was placed in a syringe for injection into the microfluidic devices (inlet A in Fig. 2). A second solution of the TIPS in hexane was placed in a second syringe (towards inlet B in Fig. 2), and both reactant solutions were injected and mixed at 1:1 ratio as explained here after. As a general rule, a colour change from yellow to dark red was observed after a certain reaction time, depending on the TIPS concentration. At room temperature, the colour change is observed after 3 minutes with $[\text{TIPS}] = 62 \text{ mM}$, whereas it is almost instantaneous with $[\text{TIPS}] = 1 \text{ M}$. Different microfluidic devices were used for each independent synthesis in order to minimize any possible contamination between experiments leading to biased observations.

The particle size distributions of the samples prepared with different TIPS concentration were determined by small angle X-ray scattering (SAXS). With very large excess of reducing agent compared to the stoichiometry ([TIPS]= 1 M), ultras-small NPs with a mean diameter of ~ 1.7 nm and a fairly narrow size distribution ($\sigma/d = 15\%$, Table S1) were quantitatively obtained (see also size distribution profile in Fig. 1). When the concentration of TIPS is lowered, a second population of nanoparticles with larger sizes (> 3 nm) is concomitantly observed (Fig. S5). The relative proportion of these larger NPs increases when the TIPS concentration is lowered (Table S1). The size distributions measured on the particles prepared with the microfluidic platform and on those prepared in batch are very similar (Tab. S1).

UV-Vis experiments

UV-Vis experiments were performed by coupling 220 μm solarization-resistant, pig-tailed multimode fiber optics (Thorlabs, US, N.A. 0.22) perpendicular to the reactor channel (Fig. 2b), in a typical Photonic lab-on-chip configuration.⁸ Input and output fiber optics were respectively coupled to a Deuterium-Halogen balanced light source AvaLight-DH-S-BAL, (Avantes, Netherlands), and a AvaSpec-2048-USB2-RM multichannel spectrometer (Avantes, Netherlands).

Specifically, the channel cross-section was designed to be 240 μm high (to host the fiber optics thickness) and 500 μm wide (providing a good compromise between a minimum optical path for a correct signal-to-noise ratio, and a maximum to keep the absorbance measurements of the studied Au(0) concentrations within the linear range). Interrogation regions, comprising self-aligning channels for hassle free and correct fiber optics positioning were conceived along the reactor, determining a given reaction time as a function of the interrogated reactor length when operating in continuous mode. Spectra were recorded in operando from 400 to 800 nm (considering the strong UV absorption of OSTEMER)⁵⁴ every 1 ms, and averaged in groups of 10 for signal improvement. When operating in stop-flow configuration, spectra could be continuously acquired and stored with a time resolution of ~ 100 ms using spectrum manufacturer's software. The possibility of using other standard and UV-compatible materials such as polydimethyl siloxane (PDMS) for the fabrication of the microreactors was excluded due to its elastic properties. The flowrates required to correctly operate the mixer would more likely induce channel deformations thus altering mixing efficiency and also optical path dimensions for an accurate UV-Vis measurement.

XAS experiments

In situ X-ray absorption spectroscopy (XAS) experiments were carried out at the SuperXAS beamline of the Swiss Light Source at the Paul Scherrer Institute in Villigen, Switzerland. XAS was conducted at the Au L_{III} -edge (covering the energy range 11 800 eV - 12 300 eV) in fluorescence mode. Time-resolved XAS signals were recorded as well on chip and in operando during the crystallization of gold nanoparticles. XAS spectra were collected using a 20 μm x 20 μm X-Ray beam and a microreactor fabricated ad-hoc, and integrating two X-ray transparent Kapton (Dupont, France) windows (75 μm thick) on the side of the OSTEMER structure configuration. The reactor was placed perpendicular to the X-ray beam (Fig. 2b). A minimum channel depth of 1,9 mm was calculated necessary to obtain a good signal-to-noise ratio for our system, whereas its width (2mm) was chosen by technical reasons to ease microreactors

manufacturing procedure. A picture and a scheme of the device can be seen in Fig. S1, and a general picture of the beamline setup is presented in Fig. S4 of the supporting information. The XAS signal was captured every 100 ms during the first 30 s of reaction by operating in continuous mode, while the signal was recorded every 3 or 4 s until the end of a reaction when operating in stop flow conditions. To obtain the information related to gold speciation as a function of time, the time-resolved XANES spectra were fitted by linear combination analysis (LCA) with three spectra as references for the Au(III), Au(I) and Au(0) oxidation states as previously reported.^{43, 49}

SAXS experiments

In situ SAXS experiments were carried out at the c-SAXS beamline of the Swiss Light Source at the Paul Scherrer Institute in Villigen, Switzerland. Like XAS studies, time-resolved SAXS signals were collected using an ad-hoc fabricated microreactor with a similar configuration. The device was analogously set perpendicularly in front of a 20 μm x 50 μm X-Ray beam, and the reactor channel (200 μm wide, with a 370 μm deep X-ray path) was probed in transmission mode with an energy of 11.5 keV. The scattered X-ray intensities were recorded at a distance of 2.17 m using a Pilatus 2M detector giving a q range from 0.01 to 0.7 \AA^{-1} . A picture and a scheme of the device can be seen in Fig. S1, and a general picture of the beamline setup is presented in Fig. S4 of the supporting information. The reactions were followed in continuous mode as a function of the probed reactor length during the first 0.3 seconds of reaction with a step resolution of ~ 100 ms, and in stop-flow between 4s and 30 min every 1 s. During the optimization experiments for the stop-flow characterizations, in some conditions, dark local depositions of gold were observed in the x-Ray beam spotted areas (not observable in lost flow operation) probably due to beam damage of the organic ligands and/or faster gold reduction caused by the energetic nature of the beam. Hence, to minimize this effect to the point that it was not visible anymore, nor detectable in the measurements, the acquisition area was programmed to change along the length of the microfluidic reactor between each stop-flow measurement.

Results

We report first the performance of the microfluidic mixer and then on the results of the in situ and real-time studies on the Au NPs synthesis obtained with successively UV-visible and X-ray absorption spectroscopy and X-ray scattering using the microfluidic platform.

Microfluidic mixer characterization

Mixer operational conditions have been screened and optimized by characterizing mixing efficiency as a function of different symmetrical reagents flowrates, by means of fluorescence measurements (Fig. 3). To this end, a fluorescein solution was mixed to D.I. water by injecting both solutions through inlets A and B using an ad-hoc fabricated syringe pump, and the intensity profile across the mixer outlet was registered as a function of the different flowrates. Considering the total volume of the butterfly structure and the reagent injection flowrates, a mixing time can be calculated and contrasted with the uniformity of the fluorescent field at the exit of the mixing structure. In optimal operational conditions, the mixer permits an efficient reagent mixing within a dead time from ~ 450 μs and down to 200 μs (as a function of the injected flowrate) for aqueous solutions.

Hence, due to the low viscosity of hexane, and the higher diffusivity of species in this media compared to water, solution homogeneity can be ensured within the previous mixing times and before any reaction occurs.

Au NP synthesis: Time-resolved, on chip UV-Vis spectrometry

The reduction of Au(III) precursor solution in Au(0) nanoparticles is reflected by a strong colour change in the visible range. The characteristic reaction times for gold nanoparticles synthesis were determined at the laboratory scale by using standard UV-Vis spectrometry. Indeed, in situ and in operando absorption spectroscopy experiments on chip allowed for tracking the influence of TIPS concentration on Au(0) NPs formation kinetics. The reaction was followed in continuous mode at a given position in the channel and subsequently the setup was switched to stop-flow configuration, the colour change from pale yellow to dark brown inside the channel, indicating the formation of Au(0) NPs. Fig. S8 shows the variation of the absorbance in the visible range during the formation of Au NPs prepared for different TIPS concentrations. An increase of the absorbance with time is observed all over the visible range but the absorbance does not exhibit the surface plasmon peak expected for Au NPs. This is explained by the very small particle size ($d_m < 2$ nm) synthesized by this method (Tab. S1). At such sizes, the surface plasmon resonance is extremely damped and the absorbance in the visible range comes from inter- and intra-band transitions of metal gold.^{55, 56}

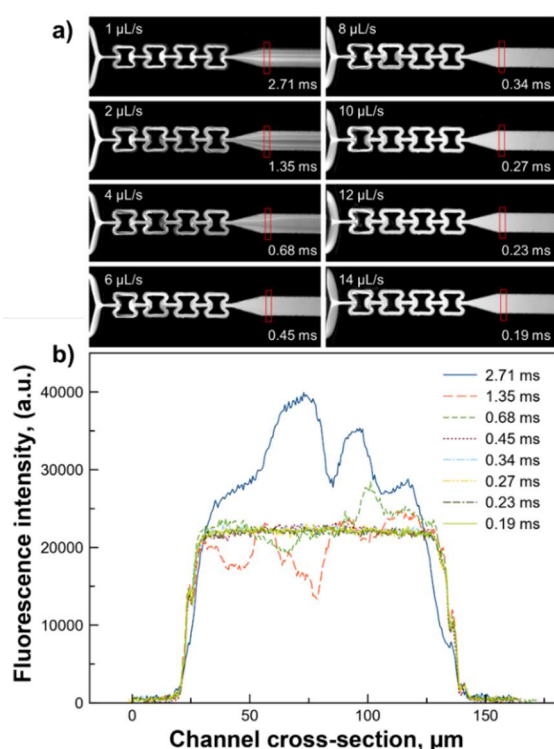


Figure 3. Characterization of the microfluidic mixer efficiency as a function of symmetrical reagent injection flowrates. a) Fluorescence images during the 1:1 mixing of a fluorescein solution with D.I. water at different flow rates, ranging from 1 to 14 $\mu\text{L s}^{-1}$. For the lower flow-rates, the inhomogeneity of the solution can be observed by the fluorescence intensity fluctuations along the microfluidic channel. b) Fluorescence intensity profile measured immediately after the mixer in the region highlighted in red for each flow rate, transduced into dead mixing times. It can be observed that for the experiments performed at flowrates from 0.45 ms (corresponding to a total injection flow rate of 8 $\mu\text{L s}^{-1}$), the fluorescence profiles are constant.

Fig. 4 shows the measured absorbance signal ($\lambda = 520$ nm) as a function of time for different TIPS concentrations. The s-shaped curves depict a first region of zero absorbance (no colour change) corresponding to an induction time region in which no Au(0) NPs formation is detected, followed by a rapid increase on the absorbance signal (burst of NP nucleation), and a long plateau corresponding to the NP growth. The differences in the latter ones, which are expected to be equal at the final synthesis stage (i.e. all syntheses were performed with the same initial amount of gold precursor) can be attributed to small differences in the optical path (small deformations of tens of microns due to the completely manual chip manufacturing process that could represent up to 10% of the total length) across the interrogation regions.

It can be clearly seen that the induction time for Au (0) NPs formation is strongly and inversely dependent on the TIPS concentration (Fig. 4b): by calculating the induction time as the intersection between the slope of the nucleation region and the initial one (baseline), the Au (0) onset varies from 185 s \pm 5 s for [TIPS] = 62 mM down to 10.5 s \pm 0.5 s for [TIPS] = 1 M.

Au NP synthesis: On-line XAS characterization

Due to the strong UV absorption of the chip fabricating material, the absorption bands of Au(III) and Au(I), corresponding to the precursor and possible intermediates oxidation states of Au(0) NPs formation,⁴³ could not be monitored by UV-Vis spectroscopy. Hence, synchrotron X-Ray absorption spectroscopy (XAS) experiments were performed to retrieve a complete picture of the Au speciation all over the reaction.

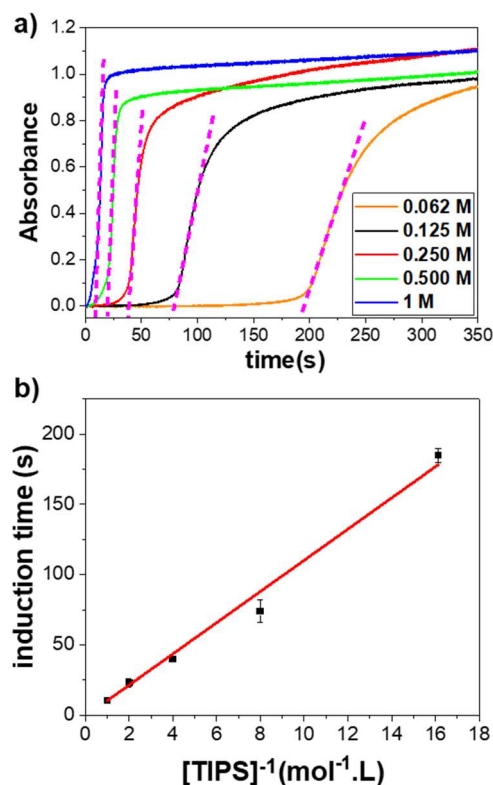


Figure 4. (a) On-chip time-resolved absorbance measurements ($\lambda = 520$ nm) during the reduction of HAuCl_4 (20 mM) with [TIPS] = 62 mM, 125 mM, 250 mM, 500 mM and 1M; Pink dashed lines represent the linear fit of the absorption slope during NPs nucleation stage, for the determination of the induction time; (b) Induction time of Au (0) formation as a function of $[\text{TIPS}]^{-1}$.

Fig. 5 shows the time-resolved variation of the gold speciation, calculated by LCA, for different Au(0) syntheses as a function of TIPS concentration, with a high level of resolution, compared to our previous observations performed in 0.75 mL cuvettes (10 mm optical path) and a 40 ms mixing dead time stop flow mixer (with a few seconds of dead time for measuring as previously discussed).⁴³

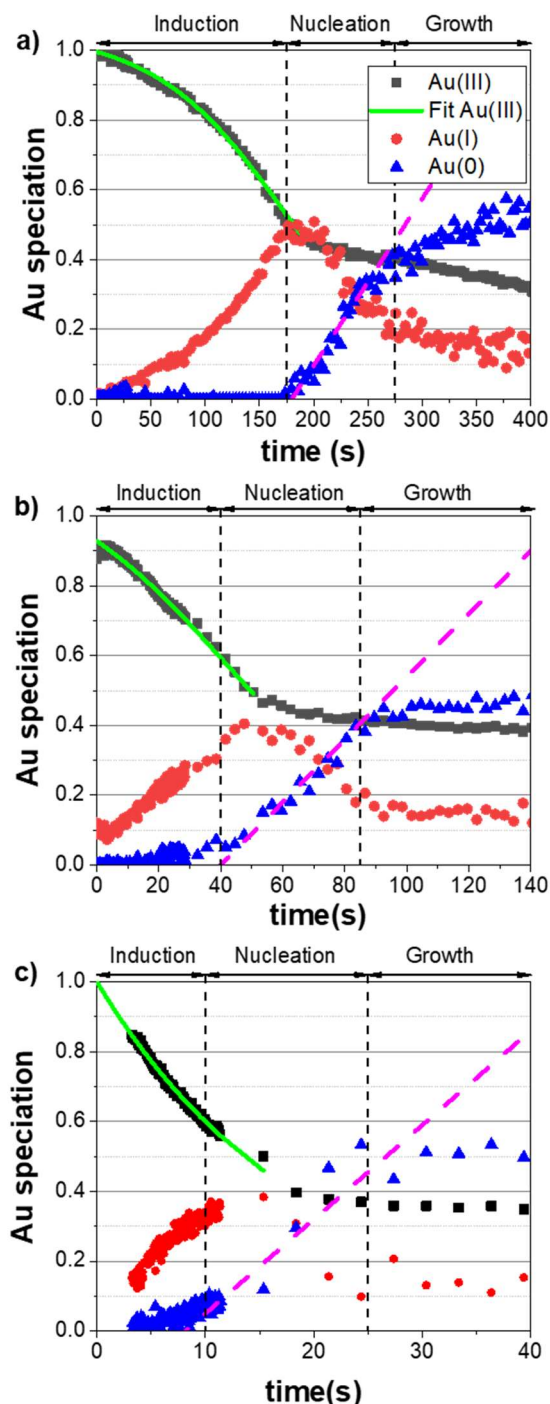


Figure 5. Relative Au(III), Au(I) and Au(0) concentrations deduced from the linear combination analysis of the XAS spectra measured in situ during the reaction using (a) [TIPS] = 62 mM, (b) 250 mM and (c) 1 M. The green lines correspond to the best fits of the [Au(III)] curves during the induction period, using an autocatalytic model for 62 and 250 mM and a 1st order reaction for 1 M (see text). The pink dashed lines are the linear fits of the first Au(0) slope for the determination of the onset time and reaction rate during the nucleation period (comprised between the two dashed lines).

As explained in the materials and methods section, the first 30 s of reaction were monitored in continuous mode (time step ~ 100 ms) to get good detail on the induction and NPs nucleation stages, whereas the subsequent data for the NPs growth stages was retrieved in stop-flow configuration, with the resolution of the XAS acquisition rate, which is about 40 times slower (~ 1s per acquisition, 3 to 4 acquisitions averaged to increase the s/n ratio). The gold speciation follows a similar trend in all the experiments, where again the same three stages observed by UV-Vis can be neatly defined: the induction period (reduction of Au(III) to Au(I)), the nucleation burst (onset and steep increase of Au(0)), and the subsequent growth stage. The variation on reaction rates and onset times for nucleation validates the general trend observed by UV-Vis: the higher the TIPS concentration, the faster the reaction is. For instance, the induction stage lasts 178 ± 2 s for [TIPS] = 62 mM but only 7.6 ± 1.0 s for [TIPS] = 1 M.

Fig. 6 shows the comparison of Au(0) formation kinetics determined by UV-Vis and XAS measurements. For every TIPS concentration probed, the agreement between the XAS and UV-Vis is remarkable. Indeed, the time-resolved information obtained at the laboratory using UV-vis absorption spectroscopy reproduce with a great fidelity the time evolution obtained from synchrotron measurements. Therefore, the direct measurement of the Au(0) concentration by UV vis is possible, providing a calibration that can be given by a complementary single Au(0) concentration measurement. XAS provides additional information about the variation of [Au(III)] and [Au(I)] during the different periods of the reaction, complementarily to the UV-Vis observations. An increase of Au(I) is observed during the induction period, reaching a maximum concentration at the Au(0) onset, in agreement with a two steps reduction Au(III)→Au(I)→Au(0). The maximum of [Au(I)] depends on the TIPS concentration. It reached 50 %, 40 % and 36 %, respectively for the 62 mM, 250 mM and 1 M [TIPS] (Fig. 5). Clearly, the nucleation stage can be defined from the onset of Au(0) to the break in the slope of Au(0) increase, as depicted in Fig. 5. The reaction rate during the nucleation stage, defined as $d[\text{Au}(0)]/dt$ and calculated from the slope of the magenta lines in Fig. 5, was found to increase linearly with the TIPS concentration (Fig. 7).

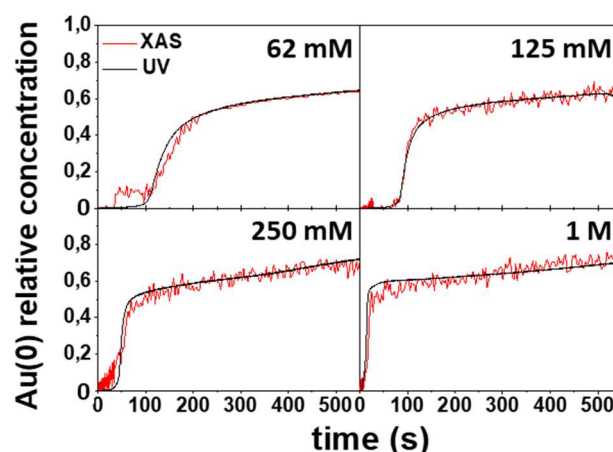


Figure 6. Comparison of relative Au(0) concentration obtained from UV-vis absorption spectroscopy and XAS for the different studied TIPS concentrations: 62 mM (upper left), 125 mM (upper right), 250 mM (lower left) and 1 M (lower right).

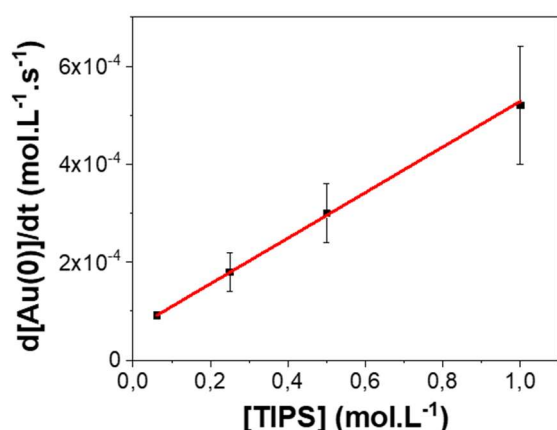
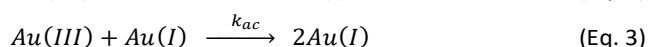
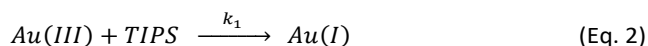


Figure 7. Reaction rate during the nucleation stage calculated as the slope of the $[Au(0)]$ increase (magenta lines in Fig. 5).

It is also noticeable in Fig. 5 and Fig. S9 that the $[Au(III)]$ curves during the induction time exhibit different curvatures depending on the TIPS concentration, they are concave for the low TIPS concentrations and convex for the high concentrations. This difference in the curvatures of $[Au(III)]$ shows a competition between two different kinetic regimes with a predominant autocatalytic regime for the low TIPS concentrations and a classical 1st order reaction for the highest TIPS concentrations.

In the supporting information we present in detail the kinetic model for the case of a competition between the direct reduction (Eq. 2) and an autocatalytic reaction (Eq. 3).



The resolution of Eq.2 alone in case of a large excess of TIPS leads to the exponential decreases of $[Au(III)]$ described by Eq. 4.

$$[Au(III)] = [Au(III)]_{\infty} + ([Au(III)]_0 - [Au(III)]_{\infty}) \exp(-k_1' t) \quad (\text{Eq. 4})$$

When both reactions are involved, the resolution of concomitant Eqs. 2 and 3 gives:

$$[Au(III)] = \frac{[Au(III)]_0 \times (k_{ac} c_0 + k_1')}{(k_{ac}[Au(III)]_0 + (k_{ac} c_0 + k_1' - k_{ac}[Au(III)]_0) \exp((k_{ac} c_0 + k_1') t))} \quad (\text{Eq. 5})$$

with $k_1' = k_1[TIPS]$, c_0 the total concentration of gold ($c_0 = 1$ after renormalization of the concentration), $[Au(III)]_0$ and $[Au(III)]_{\infty}$ the concentration of Au(III) at $t = 0$ and $t = \infty$, respectively.

The Au(III) concentration as a function of time was nicely fitted with Eq. 5 for $[TIPS] = 62 \text{ mM} - 250 \text{ mM}$ and with Eq. 4 for $[TIPS] = 1 \text{ M}$ (Fig. 5 and Fig. S9). These results show that the TIPS concentration has not only an effect on the reduction rate, it also has an influence on the competition between the direct reduction and the autocatalytic reaction during the induction stage. Note that the linear relationship between reduction rate and TIPS concentration shown in Fig. 7 does not intersect the origin, which may be explained by the existence of the second Au(III) reduction pathway of Eq. 3.

Au NP synthesis: On-line SAXS characterization

The study was completed by in situ and real time SAXS experiments. The precursor solutions obtained by dissolution of HAuCl₄ in solution of oleylamine in hexane exhibit a strong SAXS

signal that was previously interpreted by the presence of Au(III) pre-nucleation clusters (PNCs).⁴³ A mean size of around 4 nm was determined using the Beaucage model to fit the scattering signal.⁵⁷

Thanks to the microfluidic platform, the SAXS signals were obtained only 500 μs after the mixing of the Au(III) precursor solution with the TIPS solution (Fig. 8a). It is the first time that such short reaction times have been probed in this system, as the previous experiments were performed in cuvettes, inducing dead times of few seconds (typically 4s). The SAXS signals remained then fairly constant for a time period varying from $\sim 15 \text{ s}$ for $[TIPS] = 1 \text{ M}$ (Fig. 8b), $\sim 36 \text{ s}$ for $[TIPS] = 250 \text{ mM}$ and up to 3 min for 62 mM (Fig. S7). This steady-state period corresponds to the induction periods observed by UV-Vis and XAS characterizations. These new results demonstrate that the PNCs were already present in the reactive solution at these short times and did not evolve during the whole induction period (Fig. 8b and S7). Moreover, the PNCs observed all over the induction period were fairly independent of the TIPS concentration. The SAXS signals were indeed quasi similar, as revealed by Fig. 8a. The TIPS concentration had thus a strong impact on the induction time but not on the size of the PNCs.

The full in-situ SAXS signals of the reaction in the presence of different TIPS concentration are shown in the supplementary materials (Fig. S6) and complete a previous study.⁴⁹

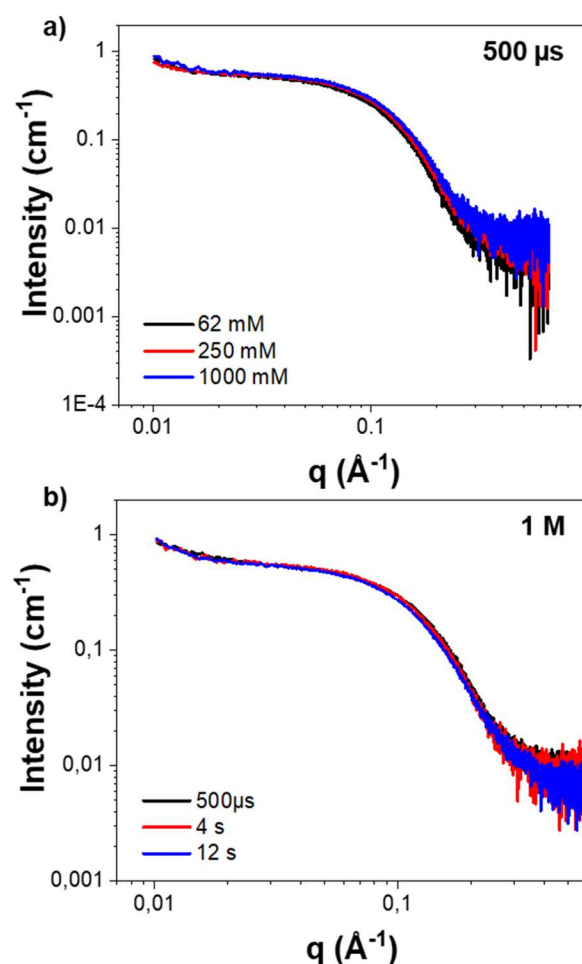


Figure 8. In situ SAXS patterns recorded (a) at $t = 500 \mu\text{s}$ for $[TIPS] = 62 \text{ mM}$ (black), 250 mM (red) and 1 M (blue line) and (b) as a function of time during the induction period for $[TIPS] = 1 \text{ M}$.

The end of the induction period and the beginning of the nucleation period are characterised/identified by a shift in the "knee position" of the SAXS signal towards higher values of q . This shift corresponds to the formation of Au NPs smaller than the initial PNCs. Then a progressive increase of the scattering intensity is observed corresponding to the increase of the Au particle size. The shift to high q corresponding to the nucleation was found to be very fast with the highest studied TIPS concentration (1 M), and more progressive for the rest of the studied conditions, in agreement with slower nucleation rates observed by UV vis and XAS (Fig. S6).

Noticeably, for the lower concentrations of TIPS, additional Bragg peaks at $q_1 = 0.1445 \text{ \AA}^{-1}$ and $q_2 = 0.289 \text{ \AA}^{-1}$ were observed during the nucleation period (Fig. S6). These peaks reveal the crystallization of a lamellar phase as intermediate. This lamellar phase, characterized by an interplane distance of 43.5 \AA was identified as an Au(I)-Cl-oleylamine compound. Therefore, for the lower TIPS concentration a competition between the fast reduction of the PNCs to Au(0) and the formation a stable intermediate Au(I) compound occurred. In contrast, a very large excess of TIPS allows favouring the direct reduction of PNCs avoiding the crystallization of the lamellar phase and eventually favouring the formation of monodisperse ultrasmall NPs.

Discussion

Kinetic analysis

The particularity of the studied system comes from the fact that the gold precursor in the presence of oleylamine forms thermodynamically (meta)stable clusters in hexane already existing prior to NPs nucleation onset (hence called prenucleation clusters). Therefore, the crystallization of the gold particles does not result from the reduction of a homogeneous solution according to a classical nucleation mechanism. Moreover, the multiple role played by the oleylamine, both as a ligand of Au(III) species for the formation of PNCs and of Au(I) species forming the lamellar phase OY-Au(I)-Cl, but also as a basic species progressively transforming into oleylammonium during the reaction (Eq.1), makes the system complex.

Thanks to the microfluidic platform, the kinetics of the reduction have been followed with a great accuracy, in particular during the induction period, and the effect of the TIPS concentration is now much better defined.

The three on-line methods (UV visible spectroscopy, XAS and SAXS) were in very good agreement for the duration of the induction period and provide complementary information. While in the induction period there is no evidence of structural evolution according to SAXS observations, we have observed that Au(III) is partially reduced to Au(I) at a rate that increases with the TIPS concentration, showing the role of TIPS in this reduction step. Additionally, a competition between two different kinetic regimes was evidenced depending on the TIPS concentration, as discussed hereunder.

For the low TIPS concentrations, a slow autocatalytic reduction is firstly observed. At the end of the induction period, when the nucleation of Au(0) starts, the relative Au(I) concentration has reached 50 % (Fig. 5a). The autocatalytic pathway for Au(I) species (Eq.3) is more prone to favour the formation of Au(I) extended arrays. Hence, a significant part of Au(I) is indeed not involved in the Au(0) nucleation but is transformed into the

relatively stable OY-Au(I)-Cl lamellar phase (Fig. S6). Consequently, two nucleation pathways are in competition, leading to a broader size distribution of the final Au NPs (Tab. S1).

For the high TIPS concentrations, a fast reduction of Au(III) to Au(I) occurs during the induction period. At the end of this period, the relative Au(I) concentration is around 40 % (Fig. 5c). No trace of lamellar phase was detected by SAXS during the reaction (Fig. S6). The fast reduction of Au(I) into Au(0) inhibits the crystallization of the lamellar phase. The nucleation step involves only the PNCs, and the final particles exhibit a narrow size distribution with a mean size of 1.7 nm (Tab. S1).

The extension of nucleation stage has been precisely defined from the Au speciation (Fig. 5). By increasing the TIPS concentration, the duration of this stage is strongly shortened and the rate of the Au(0) formation increases (Fig. 8). Despite the strong differences in the reaction rates, it is worth noting that the percentage of Au(0) involved in the nucleation stage does not vary too much, from 40 % for [TIPS] = 62 mM to 50 % for [TIPS] = 1M (Fig. 6). As mentioned above, the difference can be explained by the formation of the lamellar phase for the low TIPS concentration, which retains part of the Au(I) species. Thus, the main nucleation stage can be considered to involve only PNCs. It leads to the main population of NPs that have almost the same size, $d_m = 1.6\text{-}1.8 \text{ nm}$, independently of the TIPS concentration and therefore independently on the reaction rate (Tab. S1). This is in stark disagreement with the classical nucleation theory that relates the nucleation rate to the supersaturation threshold. These observations point out to a non-classical nucleation pathway and suggests a nucleation stage confined in the PNCs.

Several studies have reported on the Au(I)-Cl-oleylamine lamellar phase as an intermediate in the crystallisation of Au nanoparticles, with a special focus on its role in the 1D growth of ultrathin nanowires.⁵⁸⁻⁶⁰ In the present case, the lamellar phase act as a stable reservoir leading to the growth of the larger NPs with fcc structure.⁴⁹

Microreactor performance

The main features and differences of the approach here proposed, compared to other systems and methodologies reported, comes from a clear improvement in terms of time-resolved information frequency, from a few hundreds of microseconds since the beginning of the reaction and down to few tens of milliseconds in data acquisition rates, depending on the characterization technique. While other works with a similar and equally deep characterization approach can be found in literature (see e.g. the interesting work on ZnO nucleation and growth study by Herbst and coworkers⁶¹), in most of the cases the time scales related to the reaction kinetics of the systems of study are slow enough to allow a correct characterization without being constrained by mixing dead times or the limitations related to the characterization technique.

Thanks to the fast mixing, granting homogenous reaction conditions since sub-millisecond times, but also thanks to the lost flow configuration, allowing for technique independent acquisition rates, our platform permits following the evolution of fast phase transitions occurring, as in our case of study, within the first instants of a reactive precipitation. In this sense, it is also worth mentioning the differences (without entering into economical aspects) between the approach here presented, and

the already existing stop-flow commercial fast mixer units, or other fast mixers reported in literature. Regarding the dead mixing times, the microplatform would offer, in the best-case scenario, analogous performances when compared to the most advanced stop-flow devices, (e.g. estimated dead times of 200 μs for SFM 2000 series, BioLogic, France, when using microvolume cuvettes), up to 15 to 30 times higher performance when compared to the standard 3-6 ms times achieved by various current systems. If we compare the performance of the presented fast mixer with respect to other reported in literature, it is worth pointing out the main differences with respect to those attaining ultra-short mixing times on the microsecond range, and mainly oriented towards the study of protein folding-unfolding.⁶²⁻⁶⁵ In these cases, the mixing efficiency is determined by the diffusion of a reagent carried by a large stream into much smaller fluid stream jet. and local mixing efficiency is defined as the time for the proteins contained in this small jet to get in total contact with another reagent. This calculation does not take into account the global homogeneity of the mixed stream across the whole fluidic channel, which is vital to avoid local concentration fluctuations in other applications such the case here presented for reactive precipitations. Additionally, due to the very constrained dimensions of these devices, their pressure drop is much higher than that derived of the presented platforms, and their small channel depth (often in addition to the choice of fabrication materials), frequently results in very challenging, or directly impossible in-situ fine characterizations (due to the obtained signal-to-noise ratios), other than the fluorescence imaging techniques proposed in the literature, with are not universally applicable for studying phase transitions.

Above all these differences, the main advantage of the microplatform and methodology here presented is the possibility of getting rid of technique-dependent acquisition rate limitations while still consuming a relatively small amount of reagents (2.5 mL syringes were used in this work to get time-resolved information from the ms range up to several minutes, while analogous volumes were used in a previous work in a stop flow IDEX-HSP-712 mixer achieving 40 ms dead time).⁴³ This is possible due to the fact of probing stationary states as a function of the continuous reactor length (lost flow configuration), yet preserving the low consumption requirements of the microfluidic scales. Although a time resolution of ~ 100 ms has been chosen for this study, which is analogous to the resolution proposed in other lost-flow studies,⁶⁶ considering the reactor channel dimensions and the size of the probing beam for each technique, time steps could go down to, ~ 10 ms for UV-Vis or XAS measurements, and down to ~ 0.2 ms for SAXS. Additionally, due to the low Reynolds number induced by the flows at the microfluidic scale, the hydrodynamics of the 3 different reactor geometries here presented are expected to be analogous, as it has been demonstrated by the reproducibility and full agreement among the different datasets obtained with each reactor and analytical technique. Furthermore, and in contrast to other studies proposing a lost flow approach for analogous reasons,⁶⁶ the possibility of operating the microplatforms combining lost flow and stop-flow configuration, allows for a completely versatile switch between high-frequency time-resolved information for a fine characterization of short reaction times, and a classical detection configuration that permits to extend characterization times up to several hours.

Conclusions

A microreactor platform, comprising an ultra-fast micro-mixer allowing for dead times down to ~ 300 μs , and a reactor microchannel coupled to different experimental techniques (UV-Vis, XAS, SAXS), has been developed and is here proposed as a complete, novel and powerful on-chip methodology for the time-resolved study of fast reactions and phase transitions mechanisms. Thanks to a continuous flow operation, the microreactor offers the possibility of getting rid of technique-dependent acquisition rate limitations while still consuming a relatively small amount of reagents. Hence, time-resolved information can be obtained as a function of reagent flow rates, reactor channel cross section, and the size of the interrogation beam. Its distance with respect to the mixer region is transduced into a reaction time, with a time step that can be in the range of few milliseconds, down to sub-millisecond resolution when micro-beams are used. As a proof of concept, the kinetics of Au(0) ultra-small nanoparticles formation from Au(III) precursors complexed with OY in organic media, using TIPS as a reducing agent (previously studied but ill-defined), have been studied *in situ* and *in operando* with an unprecedented resolution. On-chip time-resolved SAXS experiments have allowed us to observe the presence of Au(III)/Au(I) PNCs at very short (~ 0.5 ms) reaction times and prior to the onset Au(0) formation. We observed that the PNC size and concentration are independent of the reaction conditions and remained constant during the induction period before NPs nucleation. We have also observed the formation of a transient Au(I) lamellar phase at low reducing agent concentrations during the nucleation period. Taking advantage of the highly resolved time information and the homogeneous mixing conditions, the kinetics of NPs formation were further investigated by on-chip UV-Vis measurements, in combination with time-resolved synchrotron XAS. Two different and non-classical reaction pathways leading to the formation of NPs, and associated to the presence (autocatalytic reaction) or absence (classical first-order reaction) of the Au(I) lamellar phase have been proposed and modelled.

Author Contributions

† R.K.R and E.Y. contributed equally to this work. They both should considered first authors. The manuscript was written through contributions of all authors. All authors have given approval to the final version of the manuscript.

Conflicts of interest

There are no conflicts to declare.

Acknowledgements

This project has received funding from the French ANR competitive national call (Projet NIMRod ANR-21-CE09-0019-01) and the EUR grant NanoX n° ANR-17-EURE-0009 in the framework of the « Programme des Investissements d'Avenir »,

and from the European Union's Horizon 2020 research and innovation program under grant agreement No 731019 (EUSMI). RKR has received financial support during his post-doctoral stint from Fédération FERMaT (Université de Toulouse). The authors thank PSI, Switzerland, for providing synchrotron radiation facilities at c-SAXS (Proposal No.: E190700304) and SuperXAS (Proposal No.: 20201714) as well as Dr. Adam Hugh Clark for his assistance provided for the use of the beam lines. EY thanks the Ministère de l'Enseignement Supérieur et de la Recherche et de l'Innovation for PhD funding. Angélique Gillet and Adeline Pham are warmly thanked for their help for chemical synthesis.

References

1. R. Botet and K. Roger, *Current Opinion in Colloid & Interface Science*, 2016, **22**, 108-112.
2. K. Binnemans, P. T. Jones, B. Blanpain, T. Van Gerven, Y. Yang, A. Walton and M. Buchert, *Journal of cleaner production*, 2013, **51**, 1-22.
3. O. Kašpar, A. Koyuncu, A. Pittermannová, P. Ulbrich and V. Tokárová, *Biomedical Microdevices*, 2019, **21**, 1-14.
4. J. J. De Yoreo, P. U. P. A. Gilbert, N. A. J. M. Sommerdijk, R. L. Penn, S. Whitelam, D. Joester, H. Zhang, J. D. Rimer, A. Navrotsky, J. F. Banfield, A. F. Wallace, F. M. Michel, F. C. Meldrum, H. Cölfen and P. M. Dove, *Science*, 2015, **349**, aaa6760.
5. R. Besselink, J. Rodriguez-Blanco, T. Stawski, L. G. Benning and D. Tobler, *Crystal Growth & Design*, 2017, **17**, 6224-6230.
6. S. Teychené, I. Rodriguez-Ruiz and R. K. Ramamoorthy, *Current Opinion in Colloid & Interface Science*, 2020, **46**, 1-19.
7. P. Danckwerts, *Chemical Engineering Science*, 1958, **8**, 93-102.
8. I. Rodríguez-Ruiz, T. N. Ackermann, X. Muñoz-Berbel and A. Llobera, *Analytical Chemistry*, 2016, **88**, 13, 6630-6637
9. A. Manz, N. Graber and H. á. Widmer, *Sensors and actuators B: Chemical*, 1990, **1**, 244-248.
10. T. G. Mason, J. N. Wilking, K. Meleson, C. B. Chang and S. M. Graves, *Journal of Physics: condensed matter*, 2006, **18**, R635.
11. R. Riahi, A. Tamayol, S. A. M. Shaegh, A. M. Ghaemmaghami, M. R. Dokmeci and A. Khademhosseini, *Current Opinion in Chemical Engineering*, 2015, **7**, 101-112.
12. J. Nette, P. D. Howes and A. J. deMello, *Advanced Materials Technologies*, 2020, **5**, 2000060.
13. J. B. Edel, R. Fortt, J. C. DeMello and A. J. DeMello, *Chemical communications*, 2002, 1136-1137.
14. L.-H. Hung, K. M. Choi, W.-Y. Tseng, Y.-C. Tan, K. J. Shea and A. P. Lee, *Lab on a Chip*, 2006, **6**, 174-178.
15. S. Krishnadasan, J. Tovilla, R. Vilar, A. DeMello and J. DeMello, *Journal of Materials Chemistry*, 2004, **14**, 2655-2660.
16. B. K. Yen, N. E. Stott, K. F. Jensen and M. G. Bawendi, *Advanced Materials*, 2003, **15**, 1858-1862.
17. S. Sharada, P. L. Suryawanshi, R. Kumar, S. P. Gumfekar, T. B. Narsaiah and S. H. Sonawane, *Colloids and Surfaces A: Physicochemical and Engineering Aspects*, 2016, **498**, 297-304.
18. Y. Song, C. S. Kumar and J. Hormes, *Journal of nanoscience and nanotechnology*, 2004, **4**, 788-793.
19. A. M. Karim, N. Al Hasan, S. Ivanov, S. Siefert, R. T. Kelly, N. G. Hallfors, A. Benavidez, L. Kovarik, A. Jenkins and R. E. Winans, *The Journal of Physical Chemistry C*, 2015, **119**, 13257-13267.
20. X. Z. Lin, A. D. Terepka and H. Yang, *Nano letters*, 2004, **4**, 2227-2232.
21. S. T. He, Y. L. Liu and H. Maeda, *Journal of Nanoparticle Research*, 2008, **10**, 209-215.
22. S. He, T. Kohira, M. Uehara, T. Kitamura, H. Nakamura, M. Miyazaki and H. Maeda, *Chemistry letters*, 2005, **34**, 748-749.
23. J. Wagner, T. Kirner, G. Mayer, J. Albert and J. Köhler, *Chemical Engineering Journal*, 2004, **101**, 251-260.
24. T. Ishizaka, A. Ishigaki, H. Kawanami, A. Suzuki and T. M. Suzuki, *Journal of colloid and interface science*, 2012, **367**, 135-138.
25. H. Wang, H. Nakamura, M. Uehara, M. Miyazaki and H. Maeda, *Chemical Communications*, 2002, 1462-1463.
26. Y. Song, E. Doomes, J. Prindle, R. Tittsworth, J. Hormes and C. S. R. Kumar, *The Journal of Physical Chemistry B*, 2005, **109**, 9330-9338.
27. H. Wang, X. Li, M. Uehara, Y. Yamaguchi, H. Nakamura, M. Miyazaki, H. Shimizu and H. Maeda, *Chemical communications*, 2004, 48-49.
28. V. Sebastian Cabeza, S. Kuhn, A. A. Kulkarni and K. F. Jensen, *Langmuir*, 2012, **28**, 7007-7013.
29. H. Huang, H. du Toit, S. Ben-Jaber, G. Wu, L. Panariello, N. T. K. Thanh, I. P. Parkin and A. Gavriilidis, *Reaction Chemistry & Engineering*, 2019, **4**, 884-890.
30. Q. Cai, V. Castagnola, L. Boselli, A. Moura, H. Lopez, W. Zhang, J. M. de Araújo and K. A. Dawson, *Nanoscale Horizons*, 2022, **7**, 288-298.
31. V. Hessel, S. Hardt, H. Löwe and F. Schönfeld, *AIChE Journal*, 2003, **49**, 566-577.
32. S. Hardt and F. Schönfeld, *AIChE journal*, 2003, **49**, 578-584.
33. J. B. Knight, A. Vishwanath, J. P. Brody and R. H. Austin, *Physical review letters*, 1998, **80**, 3863.
34. F. G. Bessoth, A. J. deMello and A. Manz, *Analytical communications*, 1999, **36**, 213-215.
35. A. D. Stroock, S. K. Dertinger, A. Ajdari, I. Mezic, H. A. Stone and G. M. Whitesides, *Science*, 2002, **295**, 647-651.
36. L. Wang, J.-T. Yang and P.-C. Lyu, *Chemical Engineering Science*, 2007, **62**, 711-720.
37. X. Fu, S. Liu, X. Ruan and H. Yang, *Sensors and Actuators B: Chemical*, 2006, **114**, 618-624.
38. C.-C. Hong, J.-W. Choi and C. H. Ahn, *Lab on a Chip*, 2004, **4**, 109-113.
39. S.-J. Park, J. K. Kim, J. Park, S. Chung, C. Chung and J. K. Chang, *Journal of Micromechanics and Microengineering*, 2003, **14**, 6.
40. F. Jiang, K. S. Drese, S. Hardt, M. Küpper and F. Schönfeld, *AIChE journal*, 2004, **50**, 2297-2305.
41. S. H. Wong, M. C. Ward and C. W. Wharton, *Sensors and Actuators B: Chemical*, 2004, **100**, 359-379.
42. Z. Lu, J. McMahan, H. Mohamed, D. Barnard, T. R. Shaikh, C. A. Mannella, T. Wagenknecht and T.-M. Lu, *Sensors and Actuators B: Chemical*, 2010, **144**, 301-309.
43. R. K. Ramamoorthy, E. Yildirim, E. Barba, P. Roblin, J. A. Vargas, L.-M. Lacroix, I. Rodriguez-Ruiz, P. Decorse, V. Petkov and S. Teychené, *Nanoscale*, 2020, **12**, 16173-16188.

44. X. Yin, M. Shi, J. Wu, Y.-T. Pan, D. L. Gray, J. A. Bertke and H. Yang, *Nano Letters*, 2017, **17**, 6146-6150.
45. J. K. Mathiesen, J. Quinson, S. Blaseio, E. T. S. Kjær, A. Dworzak, S. R. Cooper, J. K. Pedersen, B. Wang, F. Bizzotto, J. Schröder, T. L. Kinnibrugh, S. B. Simonsen, L. Theil Kuhn, J. J. K. Kirkensgaard, J. Rossmeisl, M. Oezaslan, M. Arenz and K. M. Ø. Jensen, *Journal of the American Chemical Society*, 2023, **145**, 1769-1782.
46. N. D. Loh, S. Sen, M. Bosman, S. F. Tan, J. Zhong, C. A. Nijhuis, P. Král, P. Matsudaira and U. Mirsaidov, *Nature chemistry*, 2017, **9**, 77-82.
47. B. Abécassis, F. Testard, Q. Kong, B. Francois and O. Spalla, *Langmuir*, 2010, **26**, 13847-13854.
48. X. Chen, J. Wang, R. Pan, S. Roth and S. Förster, *The Journal of Physical Chemistry C*, 2021, **125**, 1087-1095.
49. E. Yildirim, R. K. Ramamoorthy, R. Parmar, P. Roblin, J. A. Vargas, V. Petkov, A. Diaz, S. Checchia, I. R. Ruiz, S. Teychené, L.-M. Lacroix and G. Viau, *The Journal of Physical Chemistry C*, 2023, **127**, 3047-3058.
50. J. A. Gavira, I. Rodríguez-Ruiz, S. Martínez-Rodríguez, S. Basu, S. Teychené, A. A. McCarthy and C. Mueller-Dieckman, *Acta Crystallographica Section D: Structural Biology*, 2020, **76**, 751-758.
51. I. Rodríguez-Ruiz, S. Charton, D. Radajewski, T. Bizien and S. Teychené, *CrystEngComm*, 2018, **20**, 3302-3307.
52. T. Haraldsson, C. F. Carlborg and W. van der Wijngaart, *Proceedings Volume 8976, Microfluidics, BioMEMS, and Medical Microsystems XII*; 897608 (2014).
53. I. Rodríguez-Ruiz, S. Teychené, N. Van Pham, D. Radajewski, F. Lamadie, A. Llobera and S. Charton, *Talanta*, 2017, **170**, 180-184.
54. E. Mattio, F. Lamadie, I. Rodríguez-Ruiz, B. Cames and S. Charton, *Journal of Radioanalytical and Nuclear Chemistry*, 2020, **323**, 965-973.
55. R. Philip, P. Chantharasupawong, H. Qian, R. Jin and J. Thomas, *Nano Letters*, 2012, **12**, 4661-4667.
56. Y. Li, S. Liu, T. Yao, Z. Sun, Z. Jiang, Y. Huang, H. Cheng, Y. Huang, Y. Jiang, Z. Xie, G. Pan, W. Yan and S. Wei, *Dalton Transactions*, 2012, **41**, 11725-11730.
57. G. Beaucage, *Journal of applied crystallography*, 1996, **29**, 134-146.
58. X. Lu, M. S. Yavuz, H.-Y. Tuan, B. A. Korgel and Y. Xia, *Journal of the American Chemical Society*, 2008, **130**, 8900-8901.
59. A. Loubat, L.-M. Lacroix, A. Robert, M. Imperor-Clerc, R. Poteau, L. Maron, R. Arenal, B. Pansu and G. Viau, *The Journal of Physical Chemistry C*, 2015, **119**, 4422-4430.
60. J. A. Vargas, V. Petkov, E. S. A. Nouh, R. K. Ramamoorthy, L.-M. Lacroix, R. Poteau, G. Viau, P. Lecante and R. Arenal, *ACS nano*, 2018, **12**, 9521-9531.
61. M. Herbst, E. Hofmann and S. Förster, *Langmuir*, 2019, **35**, 11702-11709.
62. D. E. Hertzog, B. Ivorra, B. Mohammadi, O. Bakajin and J. G. Santiago, *Analytical chemistry*, 2006, **78**, 4299-4306.
63. B. Ivorra, M. R. Ferrández, M. Crespo, J. L. Redondo, P. M. Ortigosa, J. G. Santiago and Á. M. Ramos, *Journal of Mathematics in Industry*, 2018, **8**, 4.
64. S. A. Waldauer, L. Wu, S. Yao, O. Bakajin and L. J. Lapidus, *Journal of visualized experiments: JoVE*, 2012, (62), e3976.
65. D. E. Hertzog, X. Michalet, M. Jäger, X. Kong, J. G. Santiago, S. Weiss and O. Bakajin, *Analytical chemistry*, 2004, **76**, 7169-7178.
66. J. Polte, R. Erler, A. F. Thünemann, S. Sokolov, T. T. Ahner, K. Rademann, F. Emmerling and R. Kraehnert, *ACS Nano*, 2010, **4**, 1076-1082.